Effect of field spread on resting-state MEG functional network analysis: a computational modeling study

Silva Pereira[1], S., Hindriks[1], R., Mühlberg[1], S., Maris[2], E., van Ede[2], F., Griffa[3,4], A., Hagmann[3,4], P., Deco[1,5], G.

May 20, 2017

1. Center for Brain and Cognition, Computational Neuroscience Group, Department of Information and Communication Technologies, Universitat Pompeu Fabra, Barcelona, Spain.

2. Radboud University Nijmegen, Nijmegen, The Netherlands.

3. Department of Radiology, Lausanne University Hospital and University of Lausanne, 1011 Lausanne, Switzerland.

4. Signal Processing Laboratory 5, Ecole Polytechnique Federale de Lausanne, 1015 Lausanne, Switzerland.

5. Instituciò Catalana de la Recerca i Estudis Avanats (ICREA), Universitat Pompeu Fabra, Barcelona, Spain.

1

Abstract

A popular way to analyze resting-state EEG and MEG data is to treat them as a functional network in which sensors are identified with nodes and the interaction between channel time-series with the network connections. Although conceptually appealing, the network-theoretical approach to sensor-level EEG and MEG data is challenged by the fact that EEG and MEG time-series are mixtures of source activity. It is therefore of interest to assess the relationship between functional networks of source activity and the ensuing sensor-level networks. Since these topological features are of high interest in experimental studies, we address the question of to what extent the network topology can be reconstructed from sensor-level FC measures in case of MEG data. Simple simulations that consider only a small number of regions do not allow to assess network properties; therefore, we use a diffusion MRI-constrained whole-brain computational model of resting-state activity. Our motivation lies behind the fact that still many contributions found in the literature perform network analysis at sensor level, and we aim at showing the discrepancies between source- and sensor-level network topologies using realistic simulations of resting-state cortical activity. Our main findings are that the effect of field spread on network topology depends on the type of interaction (instantaneous or lagged) and leads to an underestimation of lagged FC at sensor level due to instantaneous mixing of cortical signals, instantaneous interaction is more sensitive to field spread than lagged interaction, and discrepancies are reduced when using planar gradiometers rather than axial gradiometers. We therefore recommend to use lagged interaction measures on planar gradiometer data when investigating network properties of resting-state sensor-level MEG data.

1 Introduction

Electroencephalography (EEG) and magnetoencephalography (MEG) allow for non-invasive monitoring of electrical activity in the human brain at a time-scale of milliseconds [21]. EEG and MEG have been used extensively to characterize functional connectivity (FC) underlying healthy and impaired cognitive processes, and promoted the development of methods for characterizing FC in electrophysiological recordings (EEG/MEG). Today, one can choose from a wide variety of FC measures based on different mathematical theories, such as chaotic systems, weakly-coupled oscillators, linear stochastic processes, and information theory [36, 40, 44]. In applications to EEG and MEG data, it is common practice to calculate the FC measure for all channel-pairs, resulting in an FC matrix with the corresponding one-to-one relationships. The obtained FC matrices of different subjects are subsequently analyzed and can be used to characterize different cognitive states or pathological conditions. In this study, we focus on the fundamental question of what it is that sensor-level FC matrices say about the dynamical structure of the data, and to what extent the network topology can be reconstructed from sensor-level FC measures in case of MEG data. To that end, we compare sensor-level FC matrices with the underlying cortical FC matrices.

The most common way to think about EEG/MEG FC matrices is in terms of functional networks [8, 23, 39]. Viewed as such, network nodes are assumed to correspond to cortical circuits underlying the EEG/MEG channels and network connections are assumed to correspond to functional dependencies between these circuits. Analysis of the network is typically carried out using graph-theoretic measures such as the clustering coefficient, degree distribution, and average path length. The network approach to EEG/MEG brain dynamics has demonstrated that resting-state functional networks at sensor level posses small-world properties in several frequency bands [1, 46], which would enable fast and robust integration and segregation of information [2]. Moreover, graph-theoretic measures are able to discriminate between the ongoing brain dynamics of healthy individuals and those of psychiatric and neurological patients [29, 30, 37, 38].

Although these results are encouraging and clinically relevant, by themselves they do not validate the network-theoretic view on sensor-level EEG/MEG brain dynamics. In addition, the network approach to EEG/MEG brain dynamics is questionable from a physical perspective. Concerning the physics, because EEG/MEG channels register source activity not only from tissue directly underlying the channels but from distant sources as well, they cannot directly be associated with nodes of a functional network and the FC measures suffer from spurious correlations due to the superposition of sources [22]. Moreover, scalp-based EEG connectivity estimates like vector autoregressive models have been shown to be highly affected by volume conduction [7]. To isolate true FC from spurious FC due to volume-conduction (EEG) or field spread (MEG), several approaches have been proposed. Since volume-conduction/field spread is instantaneous, an alternative is to focus on time-lagged interactions between EEG/MEG channels [26, 32, 33, 47], which necessarily reflect time-lagged interactions between sources. However, although these FC measures reduce spurious correlations and might lead to more faithful networks [5, 19, 45], it remains unclear weather such measures actually reflect functional interaction between local circuits. Another alternative is to perform a source space projection prior to calculation. Source reconstruction techniques like beamforming have become standard for source space projection of EEG/MEG sensor data, and recent studies have proposed methods to mitigate the effects of volume-conduction/field spread [10, 18, 41, 49]. Although these techniques have been shown to ease the effects of field spread, still several contributions continue applying network theory to sensor level data, and in this study we highlight the consequences of carrying out such an analysis.

Motivated by the existence of several fundamental methodological difficulties [22], we use models based on empirical data to uncover a discrepancy between cortical FC matrices and those computed at channel level. Whereas the authors in [22] focused on a single minimalistic scenario, the authors

in [10] studied the performance of a novel connectivity measure on both simulated and real data at source-level using simple networks composed of only a few nodes (five), without performing realistic simulations of resting-state cortical activity and without reporting results on sensor-level connectivity studies. The extended analysis we perform on simulated data can be contrasted with those based on a network view on EEG/MEG brain dynamics, e.g. [6,15,16,29,45,46]. To this extent, we focus on both real and complex-valued correlation measurements (or coherence), and argue that treating sensor-level resting-state EEG/MEG recordings as comprising a discrete network of interacting systems might not be appropriate and obscures rather than clarifies the true brain dynamics, since after all, the recorded electric and magnetic fields are continuous in space [42]. To demonstrate this, we use a diffusion MRI-constrained whole-brain computational model of resting-state activity, where the activity at different areas of the brain emerges through long-range synchronization of Hopf oscillators. We stress that in contrast to existing simulation studies on sensor-level FC which typically use simple network models, we perform realistic simulations based on empirical data. The measured MEG signals are obtained from a forward model assuming two different systems: sensors with axial gradiometers and sensors with planar gradiometers, the latter obtained synthetically using the Fieldtrip toolbox [35]. Then, we perform a network analysis at both source level and sensor level, and contrast the results showing that they can lead to wrong interpretations. A Louvain modularity study is included, which sheds additional light on the results from the standard network analyses performed.

2 Materials and Methods

2.1 Cortical parcellation and white-matter tractography

For the estimation of the whole-brain structural connectivity matrix S, we considered ten male healthy subjects aged 22.5 ± 1.8 years, nine right-handed and one left-handed. Each subject underwent a magnetic resonance imaging (MRI) session on a 3 Tesla scanner (Magnetom TrioTim, Siemens Medical Solutions), equipped with a 32-channel head coil. Each MRI session included a magnetization-prepared rapid acquisition gradient echo (MPRAGE) and a diffusion spectrum imaging (DSI [52]) sequence. The MPRAGE acquisition had 1 mm in-plane resolution and 1.2 mm slice thickness, covering $240 \times 257 \times 160$ voxels. The TR, TE and TI were 2300, 2.98 and 900 ms. The DSI acquisition had $2.2 \times 2.2 \times 3$ mm resolution, covering $96 \times 96 \times 34$ voxels, and it included 256 diffusion-weighted volumes (with maximum b-value 8000 s/mm^2) and one b0 volume. The TR and TE were 6100 and 144 ms. Informed written consent in accordance with institutional guidelines was obtained for all participants. Subject-wise MPRAGE volumes were segmented into white-matter, grey-matter and cerebrospinal-fluid compartments using FreeSurfer software [12], and linearly registered to the diffusion space (b0 volume) [20]. The grey-matter cortical volumes were segmented into 219 regions of interest (ROIs), according to the atlas described in [9] and using the Connectome Mapper Toolkit [11]. DSI data were reconstructed according to [52]. Deterministic streamline tractography [27] was performed on reconstructed DSI data, initiating 32 streamline propagations per voxel and per diffusion direction. A representative structural connectivity matrix S was estimated by combining tractography and cortical parcellation results from the ten subjects.

2.2 Computational model of resting-state cortical dynamics

Recently, it has been reported that the dynamics of resting-state cortical fluctuations is poised at the transition between asynchronous to oscillatory behavior [14]. We use the model proposed in [14] to simulate resting-state cortical activity, where a general neural mass model based on the normal form of a Hopf bifurcation was proposed. The model describes the dynamics of n coupled brain areas (nodes). The global dynamics emerges through the mutual interactions between the nodes, which are coupled through a connectivity matrix S. The local dynamics are modeled by the normal form of a supercritical Hopf bifurcation, which describes the transition from asynchronous noisy behavior

to self-sustained oscillations, as controlled by the bifurcation parameter, denoted a. The complex-valued cortical activity at every node j is modeled by the following set of coupled non-linear stochastic differential equations:

$$\frac{d}{dt}z_j(t) = (a + i\,\omega_0)z_j(t) - z_j(t)|z_j(t)|^2 + g\sum_{k=1}^{n} S_{j,k}\left(z_k(t - t_{j,k}) - z_j(t)\right) + \eta_j(t), \qquad (1)$$

where i is the imaginary unit, ω_0 is the intrinsic frequency, η_j is additive Gaussian white noise with intensity σ_j, and $t_{j,k}$ denotes the axonal delay between node j and node k. The parameter g globally scales the synaptic connections and is used to control the correlation between regions. When the nodes are uncoupled (i.e., $g = 0$), the local dynamics bifurcate when a crosses zero. Specifically, for $a < 0$, the local dynamics have a stable fixed point at $z_j = 0$, which corresponds to a low-activity asynchronous state due to the additive noise. For $a > 0$, there exists a stable limit-cycle with angular frequency ω_0. The effect of the bifurcation parameter value a on the local dynamics is illustrated in Fig. 1.

The complex-valued variable z_j can be decomposed into a real part x_j and imaginary part y_j as $z_j = x_j + iy_j$. In terms of x_j and y_j, Eq. (1) takes the form

$$\frac{d}{dt}x_j = ax_j - \omega_0 y_j - x_j(x_j^2 + y_j^2) + g\sum_{k=1}^{n} S_c(j,k)(x_k - x_j) + \eta_j, \qquad (2)$$

$$\frac{d}{dt}y_j = ay_j - \omega_0 x_j - y_j(x_j^2 + y_j^2) + g\sum_{k=1}^{n} S_c(j,k)(y_k - y_j) + \eta_j, \qquad (3)$$

where we have suppressed the time-dependence of x and y. Cortical activity at node j is thus modeled by the real-valued variable x_j.

To simulate realistic cortical resting-state activity, the nodes of the computational model are taken to be the ROIs in the surface-based cortical atlas described in Sec. 2.1, and the connectivity matrix is taken to be the group-averaged structural connectivity matrix obtained from diffusion MRI tractography. To obtained activity in each vertex of the cortical mesh, the activity for each ROI is copied to all vertices within that ROI. This effectively means that we assume cortical activity to be locally synchronous over several squared centimeters, which is consistent with empirical estimates of the spatial extent of cortical activity underlying resting-state EEG and MEG recordings [21, 24, 34].

From the simulated cortical activity, MEG sensor data was computed by constructing a leadfield matrix for the 275-channel MEG gradiometer system (CTF Systems Inc., Port Coquitlam, Canada) using a single-sphere head model in the Fieldtrip toolbox [35]. The source space was restricted to the vertices of the left and right Freesurfer cortical template meshes, which were manually positioned inside the MEG helmet. The single-sphere had a radius of 10 cm and was manually positioned to enclose the source space. Dipoles were assumed to be oriented perpendicular to the local cortical surface. This yielded leadfield matrices of dimensions 273×130385 for the left hemisphere and 273×131547 for the right hemisphere (the system has two reference channels not used for recording). Besides these axial gradiometer data, we computed the corresponding planar gradiometer data using Fieldtrip [35].

Noisy MEG data is obtained by adding correlated Gaussian noise to the simulated signals, for different values of the peak signal-to-noise ratio (PSNR), given by

$$PSNR = 20\log\frac{\max_{i,t}|s_i(t)|}{\sigma_N}, \qquad (4)$$

where $s_i(t)$ is the noise-free MEG signal at channel i at time t. The noise covariance matrix was obtained from an empty-room MEG recording and further scaled by a factor $\sigma_N^2/\bar{\sigma}^2$ to obtain the desired PSNR values, where $\bar{\sigma}^2$ is the mean of the entries of its main diagonal.

2.3 Functional connectivity matrices

There exist a wide range of measures to characterize functional connectivity between two simultaneously recorded time-series [36] and most of them have been applied to sensor-level EEG and MEG recordings [40]. Since EEG and MEG sensor-level time-series are linear superpositions of cortical time-series (volume-conduction/field spread), the results of sensor-level FC analyses are generally difficult to interpret. This motivated the development of FC measures that are based on time-lagged interactions, since these cannot be explained by field spread. Examples of such measures are imaginary coherency [33], phase-slope-index [32], phase-lag-index [47], and the (symmetric part of the) phase-modulation function [26]. In the current study we consider two such measures: the imaginary part of the complex-valued Pearson correlation coefficient (IC) and the phase-lag index (PLI). For comparison, we also use the real part of the (complex-valued) Pearson correlation, which quantifies instantaneous FC. Below, a short description of these three measures is given.

Given two oscillatory time-series $x = (x_1, \cdots, x_n)$ and $y = (y_1, \cdots, y_n)$, the *complex-valued Pearson correlation coefficient* $r_{x,y}$ between x and y is defined as the Pearson correlation coefficient between the analytic signals x^A and y^A of x and y, respectively. Thus, let $x^A = x + ix^H$ and $y^A = y + iy^H$ denote the analytic signals of x and y, respectively, where x^H and y^H denote the Hilbert transforms of x and y, then

$$r_{x,y} = \frac{\sum_{k=1}^n \left(x_k^A - \bar{x}^A\right)\left(y_k^A - \bar{y}^A\right)^*}{\left(\sum_{k=1}^n \left|x_k^A - \bar{x}^A\right|^2\right)^{1/2}\left(\sum_{k=1}^n \left|y_k^A - \bar{y}^A\right|^2\right)^{1/2}}, \tag{5}$$

where $\bar{x}^A$ denotes the mean of x^A, $|\cdot|$ denotes absolute value, and $(*)$ denotes complex conjugation. Note that $r_{x,y}$ is complex-valued and that $|r_{x,y}| \leq 1$, where an absolute value of 0 and 1 correspond to uncorrelated and completely correlated, respectively. Also, its angle corresponds to the phase-delay between x and y. It particular, $r_{y,x} = r_{x,y}^*$, where $*$ denotes complex conjugation. The *absolute imaginary Pearson correlation coefficient* between x and y, denoted by $r_{x,y}^{\mathrm{imag}}$, is obtained by taking the absolute value of the imaginary part of $r_{x,y}$:

$$r_{x,y}^{\mathrm{imag}} = |\mathrm{Im}(r_{x,y})|. \tag{6}$$

Similarly, the *absolute real Pearson correlation coefficient* between x and y, denoted by $r_{x,y}^{\mathrm{real}}$, is obtained by taking the absolute value of the real part of $r_{x,y}$:

$$r_{x,y}^{\mathrm{real}} = |\mathrm{Re}(r_{x,y})|. \tag{7}$$

Note that $r_{x,y}^{\mathrm{real}}$ and $r_{x,y}^{\mathrm{imag}}$ measure the instantaneous and lagged functional connectivity respectively, and take values within the interval $[0, 1]$. By calculating the real and imaginary Pearson correlation coefficients for all pairs of cortical regions, we obtained n-dimensional cortical FC matrices $\mathrm{RC}_{\mathrm{cortex}}$ and $\mathrm{IC}_{\mathrm{cortex}}$, respectively, where n is the number of cortical regions. Furthermore, by calculating the real and imaginary Pearson correlation coefficients between the time-series of every pair of MEG channels, we obtained s-dimensional sensor FC matrices, denoted by $\mathrm{RC}_{\mathrm{sensor}}$ and $\mathrm{IC}_{\mathrm{sensor}}$, respectively, where s is the number of sensors. In fact, we obtained two sensor FC matrices, corresponding to axial and planar gradiometer data.

As a third measure, we take the *phase-lag index* (PLI), which is a measure of the asymmetry of the distribution of phase-differences between x and y and takes values in the interval $[0, 1]$. A value of 0 corresponds to no coupling or instantaneous coupling (that is, phase-difference centered around $0 \mod \pi$), and a value of 1 corresponds to perfect phase locking at an angle $\neq 0 \mod \pi$ [47]. Let $\psi = (\psi_1, \cdots, \psi_n)$ denote the phase-differences between x_A and y_A The phase-lag index between x and y is then defined as

$$\rho_{x,y} = |\langle \mathrm{sign}(\psi_k) \rangle|, \tag{8}$$

6

where $\langle \cdot \rangle$ denotes the average over k. By calculating $\rho_{x,y}$ between the time-series of every pair of cortical regions or MEG sensors, we obtain FC matrices $\text{PLI}_{\text{cortex}}$ and $\text{PLI}_{\text{sensor}}$. As for the Pearson correlation coefficient, we calculated the sensor-level FC matrix for both the axial and planar gradiometer data. In the two following sections, we describe the methods we used for characterizing the FC matrices described above and for comparing corresponding cortical and sensor FC matrices.

2.4   Network analysis

We characterize and compare the topological features of the cortical and MEG sensor-level FC matrices, considering commonly used indices in MEG (and EEG) sensor-level network-theoretical studies as in e.g. [45].

Clustering coefficient: The clustering coefficient is the likelihood that neighbors of a given node will be connected to each other [51]. This measure reflects the organization of the network: whereas a random network will have clustering coefficient equal or close to 0, one with a high degree of organization (e.g. a small-world network) will have a large clustering coefficient. Consider a matrix C whose $(i,j)^{\text{th}}$ entry c_{ij} specifies the correlation measure between point i and point j. The weighted clustering index of node i is defined as

$$c_i = \frac{\sum_{k \neq i} \sum_{\substack{l \neq i \\ l \neq k}} c_{ik} c_{il} c_{kl}}{\sum_{k \neq i} \sum_{\substack{l \neq i \\ l \neq k}} c_{ik} c_{il}} \tag{9}$$

whereas the mean clustering coefficient is given by

$$c_w = \frac{1}{N} \sum_{i=1}^{N} c_i. \tag{10}$$

To highlight the differences with respect to a random network, we compute the absolute difference $|c_w - \bar{c}_w|$, where the value $\bar{c}_w$ is the clustering coefficient of a random network, which is equal to the network density.

Average path length: this measure is the average number of steps along the shortest paths for all possible pairs of nodes in the network, and is a measure of the efficiency of information transport on the network [39]. The average path length depends on the network size but does not change drastically with it. We define the length of an edge as

$$\begin{aligned} l_{ij} &= \frac{1}{c_{ij}}, && \text{if } c_{ij} \neq 0, \\ l_{ij} &= \infty, && \text{if } c_{ij} = 0 \end{aligned}$$

The average weighted path length is given by

$$l_w = \left(\frac{1}{N(N-1)} \sum_{i=1}^{N} \sum_{j \neq i}^{N} l(i,j)^{-1} \right)^{-1} \tag{11}$$

Global efficiency: efficiency is a measure of how efficiently the network exchanges information, it quantifies the exchange of information across the network. The global efficiency is computed as the average of the inverse shortest path length [39].

Communities are groups of nodes within a network that are more densely connected to one another than to other nodes. The metric modularity quantifies the quality of an assignment of nodes to communities by evaluating how much more densely connected the nodes within a community are compared to how

7

connected they would be, on average, in a random network. We consider therefore an analysis which may shed additional light on the group organization of the network: the Louvain community detection.

Louvain community detection: The Louvain method is an algorithm for detecting communities in networks that relies upon heuristics for maximizing the modularity [3]. The optimal community structure returned by the algorithm is a subdivision of the network into non-overlapping groups of nodes, such that the number of within-group edges is maximized, whereas the number of between-group edges is minimized. The size and the number of communities detected is controlled by the resolution parameter, with standard value equal to 1. Whereas resolutions higher than 1 produce larger number of clusters, resolutions lower than 1 produce lower number of clusters.

3 Results

3.1 Simulated resting-state cortical activity

We simulate resting-state cortical oscillations in the alpha frequency band (≈ 10 Hz) for a total of five minutes using the Hopf oscillators coupled through the structural connectivity matrix S, obtained from diffusion MRI fiber-tracking (see Section 2.1). We want to investigate whether there is a correlation between the FC matrices at source level and the FC matrices at sensor level; therefore, to fit the 273 sensors of the MEG helmet we choose a brain parcellation composed of $n = 219$ ROIs, listed in Table 1. Fig. 2 (a) shows the empirical structural connectivity matrix S, which exhibits a sparse connectivity, whereas Fig. 2 (b) shows the instantaneous FC matrix, denoted RC_{cortex}. Observe that the first quadrant of the matrix S contains the connectivity information from the right hemisphere, whereas the fourth contains the connectivity information from the left hemisphere. Moreover, the second and third quadrants of the matrix show the connections between the left and right hemispheres. The brain model described in Sec. 2.1 is implemented with the parameter values listed in Table 2, and a time sample of brain activity is shown in Fig. 2 (c) where different colors are used to distinguish between nodes with different activity. A seed-based RC_{cortex} matrix has been computed for the right Caudal Middle Frontal 1 region and mapped onto the different brain areas, as shown in Fig. 2 (d).

Fig. 3 (a) depicts the time series generated for 10 seconds of brain activity at one node of the brain model, and Fig. 3 (b) shows the MEG signal obtained with axial gradiometer sensors for consecutive time samples as measured at sensor level (plots are read from left to right and top to bottom). The propagation patterns observed in Fig. 3 (b) suggest a spatial organization of the relative latencies in the oscillations recorded at the different sensors. From these images we may infer that a more natural way to conceptualize sensor-level resting-state MEG brain dynamics is as a spatiotemporal continuum sampled in space and time by the channels [24]. Motivated by these observations, we investigate if a network-theoretical approach might be appropriate to characterize them.

3.2 Comparison of cortical and MEG functional networks

In this section we systematically compare the network-theoretical properties of the simulated FC matrices at the cortical- and sensor-level using the network indices described in Sec. 2.4. As outlined in Section 2.3, we use FC matrices computed using three different measures: instantaneous/real correlation (RC), lagged/imaginary correlation (IC), and the phase-lag index (PLI). Moreover, sensor-level activity is computed assuming either axial or planar gradiometer MEG sensors. After considering some general properties of the cortical and sensor functional networks in Sec. 3.2.1, we characterize and compare their clustering coefficients and global efficiency in Sections 3.2.2 and 3.2.3, respectively. Finally, in Sec. 3.2.4 we compare their community structure.

	RIGHT hemisphere		RIGHT hemisphere		LEFT hemisphere		LEFT hemisphere
1	lateralorbitofrontal 1	57	superiorparietal 4	109	lateralorbitofrontal 1	165	superiorparietal 1
2	lateralorbitofrontal 2	58	superiorparietal 5	110	lateralorbitofrontal 2	166	superiorparietal 2
3	lateralorbitofrontal 3	59	superiorparietal 6	111	lateralorbitofrontal 3	167	superiorparietal 3
4	lateralorbitofrontal 4	60	superiorparietal 7	112	lateralorbitofrontal 4	168	superiorparietal 4
5	parsorbitalis 1	61	inferiorparietal 1	113	parsorbitalis 1	169	superiorparietal 5
6	frontalpole 1	62	inferiorparietal 2	114	frontalpole 1	170	superiorparietal 6
7	medialorbitofrontal 1	63	inferiorparietal 3	115	medialorbitofrontal 1	171	superiorparietal 7
8	medialorbitofrontal 2	64	inferiorparietal 4	116	medialorbitofrontal 2	172	inferiorparietal 1
9	medialorbitofrontal 3	65	inferiorparietal 5	117	parstriangularis 1	173	inferiorparietal 2
10	parstriangularis 1	66	inferiorparietal 6	118	parsopercularis 1	174	inferiorparietal 3
11	parstriangularis 2	67	precuneus 1	119	parsopercularis 2	175	inferiorparietal 4
12	parsopercularis 1	68	precuneus 2	120	rostralmiddlefrontal 1	176	inferiorparietal 5
13	parsopercularis 2	69	precuneus 3	121	rostralmiddlefrontal 2	177	precuneus 1
14	rostralmiddlefrontal 1	70	precuneus 4	122	rostralmiddlefrontal 3	178	precuneus 2
15	rostralmiddlefrontal 2	71	precuneus 5	123	rostralmiddlefrontal 4	179	precuneus 3
16	rostralmiddlefrontal 3	72	cuneus 1	124	rostralmiddlefrontal 5	180	precuneus 4
17	rostralmiddlefrontal 4	73	cuneus 2	125	rostralmiddlefrontal 6	181	precuneus 5
18	rostralmiddlefrontal 5	74	pericalcarine 1	126	superiorfrontal 1	182	cuneus 1
19	rostralmiddlefrontal 6	75	pericalcarine 2	127	superiorfrontal 2	183	pericalcarine 1
20	superiorfrontal 1	76	lateraloccipital 1	128	superiorfrontal 3	184	lateraloccipital 1
21	superiorfrontal 2	77	lateraloccipital 2	129	superiorfrontal 4	185	lateraloccipital 2
22	superiorfrontal 3	78	lateraloccipital 3	130	superiorfrontal 5	186	lateraloccipital 3
23	superiorfrontal 4	79	lateraloccipital 4	131	superiorfrontal 6	187	lateraloccipital 4
24	superiorfrontal 5	80	lateraloccipital 5	132	superiorfrontal 7	188	lateraloccipital 5
25	superiorfrontal 6	81	lingual 1	133	superiorfrontal 8	189	lingual 1
26	superiorfrontal 7	82	lingual 2	134	superiorfrontal 9	190	lingual 2
27	superiorfrontal 8	83	lingual 3	135	caudalmiddlefrontal 1	191	lingual 3
28	caudalmiddlefrontal 1	84	fusiform 1	136	caudalmiddlefrontal 2	192	lingual 4
29	caudalmiddlefrontal 2	85	fusiform 2	137	caudalmiddlefrontal 3	193	fusiform 1
30	caudalmiddlefrontal 3	86	fusiform 3	138	precentral 1	194	fusiform 2
31	precentral 1	87	fusiform 4	139	precentral 2	195	fusiform 3
32	precentral 2	88	parahippocampal 1	140	precentral 3	196	fusiform 4
33	precentral 3	89	entorhinal 1	141	precentral 4	197	parahippocampal 1
34	precentral 4	90	temporalpole 1	142	precentral 5	198	entorhinal 1
35	precentral 5	91	inferiortemporal 1	143	precentral 6	199	temporalpole 1
36	precentral 6	92	inferiortemporal 2	144	precentral 7	200	inferiortemporal 1
37	paracentral 1	93	inferiortemporal 3	145	precentral 8	201	inferiortemporal 2
38	paracentral 2	94	inferiortemporal 4	146	paracentral 1	202	inferiortemporal 3
39	paracentral 3	95	middletemporal 1	147	paracentral 2	203	inferiortemporal 4
40	rostralanteriorcingulate 1	96	middletemporal 2	148	rostralanteriorcingulate 1	204	middletemporal 1
41	caudalanteriorcingulate 1	97	middletemporal 3	149	caudalanteriorcingulate 1	205	middletemporal 2
42	posteriorcingulate 1	98	middletemporal 4	150	posteriorcingulate 1	206	middletemporal 3
43	posteriorcingulate 2	99	bankssts 1	151	posteriorcingulate 2	207	middletemporal 4
44	isthmuscingulate 1	100	superiortemporal 1	152	isthmuscingulate 1	208	bankssts 1
45	postcentral 1	101	superiortemporal 2	153	postcentral 1	209	bankssts 2
46	postcentral 2	102	superiortemporal 3	154	postcentral 2	210	superiortemporal 1
47	postcentral 3	103	superiortemporal 4	155	postcentral 3	211	superiortemporal 2
48	postcentral 4	104	superiortemporal 5	156	postcentral 4	212	superiortemporal 3
49	postcentral 5	105	transversetemporal 1	157	postcentral 5	213	superiortemporal 4
50	supramarginal 1	106	insula 1	158	postcentral 6	214	superiortemporal 5
51	supramarginal 2	107	insula 2	159	postcentral 7	215	transversetemporal 1
52	supramarginal 3	108	insula 3	160	supramarginal 1	216	insula 1
53	supramarginal 4			161	supramarginal 2	217	insula 2
54	superiorparietal 1			162	supramarginal 3	218	insula 3
55	superiorparietal 2			163	supramarginal 4	219	insula 4
56	superiorparietal 3			164	supramarginal 5		

Table 1: Brain parcellation composed of 219 ROIs.

Parameter	symbol	value
Number of areas	n	219
Bifurcation parameter	a	10
Global coupling constant	g	50-100
Areal oscillation frequency	f_0	10 ± 1 Hz
Areal noise intensity	σ	1×10^{-3}
sampling frequency	f_s	100 Hz
time	t	300 s
peak SNR of MEG data	PSNR	$0 - 30$ dB

Table 2: Parameters of the cortical Hopf model, their symbols, and nominal values.

3.2.1 General properties

Fig. 4(a)-(c) show the cortical FC matrices RC_{cortex}, IC_{cortex}, PLI_{cortex}, and the ensuing sensor FC matrices RC_{sensor}, IC_{sensor}, PLI_{sensor}, for both axial (Fig. 4(d)-(f)) and planar (Fig. 4(g)-(i)) gradiometer MEG sensors. Moreover, Fig. 4(j)-(l) depict the distributions of FC values for each of the three FC types. We can make a number of observations. First, notice that the RC cortical FC exhibits a similar structure than IC and PLI cortico FC, but significanlty higher values. Furthermore, this is approximately true for the sensor activity as well, which agrees with experimental observations [33]. It means that latencies between oscillations at different areas or sensors are much smaller than the oscillation period (which is about 100 ms for alpha oscillations). Lagged cortical FC (IC and PLI) values, however, are larger than lagged sensor FC values, which means that sensor FC matrices underestimate lagged FC. The main cause of this reduction in lagged FC is the instantaneous mixing of cortical signals through field spread. This phenomena is not unique to MEG recordings but can be observed in EEG and local field potential (LFP) recordings as well [25]. Second, lagged functional networks as measured with PLI are sparser than as measured with IC, and the distribution of their values is less spread for the planar gradiometer system.

Concerning the gradiometer type, notice that the instantaneous functional network (RC) is sparser for planar gradiometers (Fig. 4(g)) than for axial gradiometers (Fig. 4(d)). This is to be expected since planar gradiometers yield the highest signal intensities right above active cortical tissue and integrate source activity over smaller regions of cortex [21]. We observe that the matrices at sensor level (Fig. 4 (d)-(i)) show more modularity and a higher level of organization, and as expected, from the first column (Fig. 4(a), (d), (g)) we can see that the real correlation matrix RC is more sensitive to field spread.

3.2.2 Topology of resting-state networks I: MEG axial gradiometers

The network indices computed from the FC matrices at source level are compared here with those obtained from the FC matrices at sensor level assuming the MEG system with axial gradiometers. In order to do so, we apply a threshold and compute the binary FC matrices to analyze their organization structure for different threshold values. Fig. 5 (a) shows the clustering coefficient for RC computed with (9) as a function of the binarization threshold, along with the density. Observe that for values in the range $[0.2, 0.9]$ the clustering coefficient of RC_{sensor} exhibits a sort of flooring effect, showing that, although the total number of connections decreases, the number of 3-dimensional cliques remains almost unchanged within that range. This is equivalent to say that the links connecting three nodes are robust. However, this effect is not observed in the RC_{cortex} where the clustering coefficient curve shows a decreasing trend more similar to the one for the density at sensor level. Fig. 5 (b) shows the absolute difference $|c_w - \bar{c}_w|$ for both RC_{cortex} and RC_{sensor}, where $\bar{c}_w$ denotes the average clustering coefficient of a random network, which in this case is equal to the density. In other words, this measure quantifies the difference in clustering with respect to a random network. The larger the value obtained

is, the higher the organization of the network (for that particular threshold value). We identify (and highlight) an *optimum* value for each curve, which clearly do not coincide at source and at sensor level. Fig. 5 (c) shows the efficiency of the network as a function of the binarization threshold. Again, the efficiency computed for RC_{cortex} evidences a different organization than the one for RC_{sensor}. From these results we can infer that RC_{sensor} exhibits a higher level of organization than RC_{cortex} for values above 0.35, or equivalently, less randomness. Different results are obtained for IC and PLI matrices, where both IC_{cortex} and PLI_{cortex} exhibit larger clustering coefficients than those at source level in IC_{sensor} and PLI_{sensor}. Note that the FC matrix exhibiting largest distance with respect to a random network in this case is PLI_{sensor} followed by PLI_{cortex}, as shown in Fig. 5 (e). On the other hand, the global efficiency for these matrices is highest for IC_{cortex} (see Fig. 5 (f)), followed by PLI_{cortex}.

The results presented so far are obtained considering noise-free measurements. To asses the impact of measurement noise, we perform simulations for several values of PSNR, as defined in (4). Fig. 6 plots the results vs. PSNR values in the range $[0, 30]$ dB: (a) and (b) show respectively the clustering coefficient and the global efficiency vs. PSNR for the real correlation matrix RC_{sensor}, along with the results for its randomized counterparts, obtained by randomly shuffling the entries of the upper triangular part of the matrix. Fig. 6 (c) and (d) show the same results for IC and PLI. As expected, the clustering coefficient is slightly larger for the FC matrices than their random versions in all cases, while the global efficiency is slightly higher for the random versions in all the PSNR spectrum. In all cases, we observe that the network indices increase with high PSNR, with a clear transition starting from 10 dB. These incremental behaviors are also observed in the number of communities detected, as explained in Sec. 3.2.4.

3.2.3 Topology of resting-state networks II: MEG planar gradiometers

In this section we compare the network indices assuming the MEG system with planar gradiometers. Fig. 7 (a) shows the clustering coefficient for RC_{cortex} and RC_{sensor} as functions of the binarization threshold. For the sake of clarity, we include again the curve for the density. Moreover, Fig. 7 (b) shows the absolute difference $|c_w - \bar{c}_w|$ computed for both RC_{cortex} and RC_{sensor}. As expected, the results obtained for the RC matrices are similar to those obtained with the axial gradiometer sensors, whereas the results for IC and PLI matrices are slightly different. In Fig. 7 (e) we can see that in this case, IC_{cortex} and PLI_{cortex} show less distance with respect to a random network than IC_{sensor} and PLI_{sensor}. Regarding noisy data, Fig. 8 (a) and (b) show the clustering coefficient and the global efficiency vs. PSNR in the range $[0, 30]$ for the real correlation matrices RC, along with the results for their randomized counterparts. Fig. 8 (c) and (d) show the same results for IC and PLI at both source and sensor level. The clustering coefficient and the efficiency increase with PSNR for all FC matrices. From Fig. 8 (c) and (d) we can see that both the clustering coefficient and the global efficiency are higher for IC_{sensor} than for PLI_{sensor}. From all the results presented, we can infer that the FC matrices at sensor level show a different level of organization than the FC matrices at source level, independently of the gradiometer system used.

3.2.4 Community structure

The Louvain modularity analysis performed for all FC matrices and assuming different values of the resolution parameter yields more interesting results. Table 3 lists the number of detected communities for each network assuming the standard value of the resolution parameter (i.e., 1), and Fig. 9 provides a graphical representation of these results, where the nodes belonging to the same community are rearranged and the communities are reordered by size within the respective matrix. Note that a large number of communities at the cortex are composed of only a few elements, whereas at sensor level, the planar matrices have a smaller number of communities (last row of Fig. 9). Moreover, the axial IC_{sensor} and PLI_{sensor} have a large number of communities with only one element. Fig. 10 shows the results of mapping the Louvain communities detected onto the MEG helmet, where only the most six

11

$RC_{cortex} = 28$	$IC_{cortex} = 18$	$PLI_{cortex} = 20$
RC_{sensor} axial $= 6$	IC_{sensor} axial $= 51$	PLI_{sensor} axial $= 28$
RC_{sensor} planar $= 4$	IC_{sensor} planar $= 14$	PLI_{sensor} planar $= 8$

Table 3: Number of communities detected for each FC matrix.

significant communities are highlighted in colors (the remaining communities are all colored in black). The first row of Fig. 10 depicts the distribution of communities for RC_{sensor}, IC_{sensor} and PLI_{sensor} for the MEG system with axial gradiometer sensors, whereas the second row shows the distribution of communities for RC_{sensor}, IC_{sensor} and PLI_{sensor} assuming the MEG system with planar gradiometer sensors. Except for the case of RC (first column of Fig. 10), no particular patterns can be identified for the imaginary correlation matrices, and the communities seem to follow a radial distribution rather than a well-defined network. These images reveal that we should be careful in order not to draw wrong conclusions about the underlying structure of the brain.

We investigate next the impact of the resolution parameter of the Louvain method on the number of detected communities for all matrices. Fig. 11 (a) depicts the number of communities detected as a function of the resolution parameter in the range $[0.5, 1.5]$ for all FC matrices with the axial gradiometer system, where the results have been obtained averaging 500 independent realizations. Analogously, Fig. 11 (b) shows the results obtained with the planar gradiometer system. As expected, the number of communities detected increases with increasing resolution parameter in both cases. Except for RC, the number of communities detected at the cortex is smaller than the number of communities detected at sensor level, and this difference is more evident for RC and PLI matrices in both MEG systems. The difference at source and sensor level for RC remains almost constant for the entire resolution range for the axial gradiometer system. This might be interpreted as the planar system having a greater impact on the RC measures as the resolution parameter of the algorithm is increased, and less on the IC measures.

From these results we can see that, increasing the resolution we systematically obtain a larger number of communities for all matrices. We can also observe that the number of communities is larger at sensor level than at source level for lagged correlations, as shown by the curves. The implications of the results in Fig. 11 (a)-(b) are: first, we observe a discrepancy between the community structure of cortical resting-state activity and that of the ensuing sensor level measurements (namely a different number of communities). Second, it shows that this discrepancy is systematic, that is, at source level the number of communities is always larger than at sensor level. Third, this observation holds for lagged FC matrices (IC and PLI) and different gradiometer systems (axial/planar).

Analyzing the impact of noise in the number of detected communities, we observe from Fig. 11 (c)-(d) that noise has greater impact on the IC_{sensor}, as more communities are detected with higher PSNR for both systems. The impact of noise is lower for RC_{cortex}, where the number of communities detected does not change significantly with PSNR.

4 Discussion

A common way to conceptualize and analyze sensor-level EEG and MEG resting-state data is in terms of functional networks [1, 4, 19, 29, 38, 43, 45, 46]. In this approach, the nodes of the network correspond to EEG or MEG sensors and (the strength of its) links correspond to the estimated values of an interaction measure between the time-series recorded at the corresponding nodes. The functional network is subsequently analyzed using graph-theoretical indices [8, 23, 39]. Although the network-theoretical approach to sensor-level EEG/MEG data is potentially interesting since resting-state cortical dynamics is known to be comprised of a number of functional networks [1, 2, 46], it is not without methodolog-

ical challenges [28, 50]. One of these challenges, which has received surprisingly little attention, is the fact that EEG/MEG record linear superpositions of cortical activity [21]. Although this nature of EEG/MEG signals has motived the development of interaction measures that are less affected by volume-conduction/field spread [7, 26, 32, 33, 47], as well as the use of source reconstruction using techniques such as beamforming [10, 18, 41, 49], surprisingly few studies have investigated the relationship between cortical and sensor-level EEG/MEG networks [22, 41], despite the fact that these topological features are of high interest in experimental studies [4–6, 15, 16, 19, 29, 45, 46]. Moreover, simple simulations that consider only a small number of regions do not allow to assess network properties. In this study we used a whole-brain computational modeling approach to resting-state dynamics [13] to compare cortical and sensor-level resting-state MEG networks, and considering two different MEG systems: sensors with axial gradiometers and sensors with planar gradiometers. In our simulations, we included both instantaneous interaction, as measured by real-valued correlation, as well as lagged interaction, as measured by imaginary-valued correlation and the phase lag index (PLI) [47]. In addition to the commonly studied network measures, we performed a Louvain community analysis and we studied the impact of noise in the measurements using empty-room MEG recordings. Below, we discuss our main findings and their implications for network-based analysis of MEG sensor-level data.

One of our main findings is that the effect of field spread on network topology depends on the type of interaction (instantaneous or lagged), measured by different interaction measures. This holds both for the magnitude of the effect as well as for how field spread changes network topology. In particular, instantaneous correlations are more susceptible for field spread than lagged correlations, which is not surprising because field spread is instantaneous [21]. In fact, the interaction measures that have been proposed to deal with volume-conduction or field spread [26, 32, 33, 47] all are based on lagged correlations, in one way or another. But field spread also affects instantaneous and lagged interaction in different ways: for instantaneous interaction, it leads to a "flooring" of the mean clustering coefficient and global efficiency (as a function of binarization threshold) and to an increased threshold for maximal distance to a random network. For lagged interaction, the mean clustering coefficient and global efficiency descrease (for any given threshold). Thus, our simulations suggest that lagged interactions are more easily assessed from sensor-level MEG data, a finding that generalizes previous studies [26, 32, 33, 47] to large-scale functional networks.

The Louvain community analysis yields interesting results. First of all, at source level there is a large number of modules with few elements, a particularity not observed at sensor level. For imaginary correlation (IC) and phase-lag index (PLI) at source level there is only one big community. These organizations do not reflect the coupling among nodes due to the structural connectivity matrix, but rather reflect the spatial low-pass properties of the MEG forward model. The same effect is captured by the axial system at sensor level. On the other hand, a significantly smaller number of communities is detected by the algorithm for the planar system, which may lead to the conclusion of a more organized underlying structure. In general, the number of communities at source and sensor level do not match, and the results suggest a different structural organization of the functional connectivity (FC) matrices. Similar conclusions can be drawn from the case of noisy MEG measurements: as the peak signal-to-noise (PSNR) increases, the number of communities increases and the results approach the noise-free case. Regarding the network indices studied, their values are also affected by noise, showing a discrepancy with respect to the noise-free case.

Another main finding is that the discrepancy between (sensor-level) MEG and cortical networks is larger when using axial gradiometers than when using planar gradiometers. This holds for both instantaneous and lagged interaction and for all studied network-theoretical measures (mean clustering coefficient, network density, average path-length, and global efficiency). Most network-theoretical studies using sensor-level MEG, however, have used axial gradiometers [1, 5, 17, 45], and (as far as we know), (virtual) planar gradiometers have not yet been used for this purpose. To understand why planar gradiometer data is less affected by field spread, recall that the (virtual) planar transformation

is the sum of the squared magnetic fluxes through two perpendicular directions that are (approximately) perpendicular to the skull. This transformation, which is called the Laplacian, behaves like a spatial high-pass filter. It hence reduces the MEG sensor's sensitivity to distant sources because the source's magnetic fields contains predominantly low spatial frequencies. In contrast to MEG studies, the Laplacian has been used frequently applied to (scalp) EEG data [48] as well as to local field potential recordings [25, 31] to increase spatial resolution. Based on our findings, we recommend using (virtual) planar gradiometer data when assessing network properties from sensor-level MEG data.

5   Conclusions

Functional networks constitute a common way to conceptualize and analyze sensor-level EEG and MEG resting-state data, in which sensors are identified with nodes and the interaction between channel time-series with the network connections. The network-theoretical approach is however challenged by the fact that EEG and MEG time-series are mixtures of source activity. Since still many contributions found in the literature perform network analysis at sensor level, in this study we address the question of to what extent the network topology can be reconstructed from sensor-level FC measures in case of MEG data. Using a diffusion MRI-constrained whole-brain computational model of resting-state cortical activity, we report discrepancies between source- and sensor-level network topologies, and observe that the effect of field spread on network topology depends on the type of interaction (instantaneous or lagged). Moreover, we found that instantaneous interaction is more sensitive to field spread than lagged interaction, and that the discrepancies are reduced when using planar gradiometers rather than axial gradiometers. We therefore recommend to use lagged interaction measures on planar gradiometer data when investigating network properties of resting-state sensor-level MEG data.

Acknowledgements

References

[1] Danielle S. Bassett, Andreas Meyer-Lindenberg, Sophie Achard, Thomas Duke, and Edward Bullmore. Adaptive reconfiguration of fractal small-world human brain functional networks. *Proceedings of the National Academy of Sciences*, 103(51):19518–19523, 2006.

[2] Danielle Smith Bassett and Ed Bullmore. Small-world brain networks. *Neuroscientist*, 12(6):512–23, December 2006.

[3] Vincent D Blondel, Jean-Loup Guillaume, Renaud Lambiotte, and Etienne Lefebvre. Fast unfolding of communities in large networks. *Journal of Statistical Mechanics: Theory and Experiment*, 2008(10):P10008, 2008.

[4] Maria Boersma, Dirk J a Smit, Henrica M a de Bie, G Caroline M Van Baal, Dorret I Boomsma, Eco J C de Geus, Henriette a Delemarre-van de Waal, and Cornelis J Stam. Network analysis of resting state EEG in the developing young brain: structure comes with maturation. *Hum. Brain Mapp.*, 32(3):413–25, March 2011.

[5] Ingeborg Bosma, Jaap C Reijneveld, Martin Klein, Linda Douw, Bob W van Dijk, Jan J Heimans, and Cornelis J Stam. Disturbed functional brain networks and neurocognitive function in low-grade glioma patients: a graph theoretical analysis of resting-state MEG. *Nonlinear Biomed. Phys.*, 3(1):9, 2009.

[6] Matthew J. Brookes, Prejaas K. Tewarie, Benjamin A.E. Hunt, Sian E. Robson, Lauren E. Gascoyne, Elizabeth B. Liddle, Peter F. Liddle, and Peter G. Morris. A multi-layer network approach to {MEG} connectivity analysis. *NeuroImage*, 132:425 – 438, 2016.

[7] C. Brunner, M. Billinger, M. Seeber, T. R. Mullen, and S. Makeig. Volume conduction influences scalp-based connectivity estimates. *Frontiers in Computational Neuroscience*, 10:121, 2016.

[8] Ed Bullmore and Olaf Sporns. Complex brain networks: graph theoretical analysis of structural and functional systems. *Nat. Rev. Neurosci.*, 10(3):186–98, March 2009.

[9] Leila Cammoun, Xavier Gigandet, Djalel Meskaldji, Jean Philippe Thiran, Olaf Sporns, Kim Q. Do, Philippe Maeder, Reto Meuli, and Patric Hagmann. Mapping the human connectome at multiple scales with diffusion spectrum {MRI}. *Journal of Neuroscience Methods*, 203(2):386 – 397, 2012.

[10] G.L. Colclough, M.J. Brookes, S.M. Smith, and M.W. Woolrich. A symmetric multivariate leakage correction for {MEG} connectomes. *NeuroImage*, 117:439 – 448, 2015.

[11] Alessandro Daducci, Stephan Gerhard, Alessandra Griffa, Alia Lemkaddem, Leila Cammoun, Xavier Gigandet, Reto Meuli, Patric Hagmann, and Jean-Philippe Thiran. The connectome mapper: An open-source processing pipeline to map connectomes with mri. *PLoS ONE*, 7(12):1–9, 12 2012.

[12] Anders M. Dale, Bruce Fischl, and Martin I. Sereno. Cortical Surface-Based Analysis: I. Segmentation and Surface Reconstruction. *NeuroImage*, 9(2):179 – 194, 1999.

[13] Gustavo Deco, Viktor K. Jirsa, and Anthony R. McIntosh. Emerging concepts for the dynamical organization of resting-state activity in the brain. *Nature Reviews Neuroscience*, 12(1):43–56, 01 2011.

[14] Gustavo Deco, Morten L. Kringelbach, Viktor K. Jirsa, and Petra Ritter. The dynamics of resting fluctuations in the brain: metastability and its dynamical cortical core. *Submitted to*, 2016.

[15] Matteo Demuru, Francesca Fara, and Matteo Fraschini. Brain network analysis of eeg functional connectivity during imagery hand movements. *Journal of Integrative Neuroscience*, 12(04):441–447, 2013. PMID: 24372064.

[16] Lorena Deuker, Edward T Bullmore, Marie Smith, Soren Christensen, Pradeep J Nathan, Brigitte Rockstroh, and Danielle S Bassett. Reproducibility of graph metrics of human brain functional networks. *Neuroimage*, 47(4):1460–8, October 2009.

[17] L. Douw, M.M. Schoonheim, D. Landi, M.L. van der Meer, J.J.G. Geurts, J.C. Reijneveld, M. Klein, and C.J. Stam. Cognition is related to resting-state small-world network topology: an magnetoencephalographic study . *Neuroscience*, 175:169 – 177, 2011.

[18] M. Drakesmith, W. El-Deredy, and S. Welbourne. Reconstructing Coherent Networks from Electroencephalography and Magnetoencephalography with Reduced Contamination from Volume Conduction or Magnetic Field Spread. *PLOS ONE*, 8(12):1–17, 12 2013.

[19] Fabrizio De Vico Fallani, Floriana Pichiorri, Giovanni Morone, Marco Molinari, Fabio Babiloni, Febo Cincotti, and Donatella Mattia. Multiscale topological properties of functional brain networks during motor imagery after stroke. *NeuroImage*, 83:438 – 449, 2013.

[20] Douglas N. Greve and Bruce Fischl. Accurate and robust brain image alignment using boundary-based registration. *NeuroImage*, 48(1):63 – 72, 2009.

[21] M. Hamalainen, R. Hari, J. Ilmoniemi, J. Knuutila, and O.V. Lounasmaa. Magnetoencephalography—theory, instrumentation, and applications to noninvasive studies of the working human brain. *Rev. Mod. Phys.*, 65(2), 1993.

[22] Stefan Haufe, Vadim V. Nikulin, Klaus-Robert Mller, and Guido Nolte. A critical assessment of connectivity measures for {EEG} data: A simulation study. *NeuroImage*, 64:120 – 133, 2013.

[23] Yong He and Alan Evans. Graph theoretical modeling of brain connectivity. *Curr. Opin. Neurol.*, 23(4):341–50, August 2010.

[24] R. Hindriks, M. J. A. M. van Putten, and G. Deco. Intra-cortical propagation of EEG alpha oscillations. *Neuroimage*, 103:444–53, December 2014.

[25] Rikkert Hindriks, Xerxes D. Arsiwalla, Theofanis Panagiotaropoulos, Michel Besserve, Paul F. M. J. Verschure, Nikos K. Logothetis, and Gustavo Deco. Discrepancies between Multi-Electrode LFP and CSD Phase-Patterns: A Forward Modeling Study. *Frontiers in Neural Circuits*, 10:51, 2016.

[26] Rikkert Hindriks, Fetsje Bijma, Bob W. van Dijk, Cornelis J. Stam, Ysbrand Y. van der Werf, Eus J W van Someren, Jan C. de Munck, and Aad W. van der Vaart. Data-driven modeling of phase interactions between spontaneous MEG oscillations. *Hum. Brain Mapp.*, 32(7):1161–1178, 2011.

[27] Derek K. Jones. Studying connections in the living human brain with diffusion {MRI}. *Cortex*, 44(8):936 – 952, 2008. Special Issue on Brain Hodology – Revisiting disconnection approaches to disorders of cognitive function:

[28] Amir Joudaki, Niloufar Salehi, Mahdi Jalili, and Maria G Knyazeva. EEG-based functional brain networks: does the network size matter? *PLoS One*, 7(4):e35673, January 2012.

[29] Dae-Jin Kim, Amanda R Bolbecker, Josselyn Howell, Olga Rass, Olaf Sporns, William P Hetrick, Alan Breier, and Brian F O'Donnell. Disturbed resting state EEG synchronization in bipolar disorder: A graph-theoretic analysis. *NeuroImage. Clin.*, 2:414–23, January 2013.

[30] Sifis Micheloyannis, Ellie Pachou, Cornelis Jan Stam, Michael Breakspear, Panagiotis Bitsios, Michael Vourkas, Sophia Erimaki, and Michael Zervakis. Small-world networks and disturbed functional connectivity in schizophrenia. *Schizophr. Res.*, 87(1-3):60–6, October 2006.

[31] U. Mitzdorf. Current source-density method and application in cat cerebral cortex: investigation of evoked potentials and EEG phenomena. *Physiological Reviews*, 65(1):37–100, 1985.

[32] G. Nolte, A. Ziehe, V. V. Nikulin, A. Schlögl, N. Krämer, T. Brismar, and K.R. Müller. Robustly estimating the flow direction of information in complex physical systems. *Phys. Rev. Lett.*, 100:234101, Jun 2008.

[33] Guido Nolte, Ou Bai, Lewis Wheaton, Zoltan Mari, Sherry Vorbach, and Mark Hallett. Identifying true brain interaction from EEG data using the imaginary part of coherency. *Clin. Neurophysiol.*, 115(10):2292–307, October 2004.

[34] P. L. Nunez and R. Srinivasan. A theoretical basis for standing and traveling brain waves measured with human EEG with implications for an integrated consciousness. *Clin. Neurophysiol.*, 117(11):2424–35, November 2006.

[35] R. Oostenveld, P. Fries, E. Maris, and J.M. Schoffelen. FieldTrip: Open Source Software for Advanced Analysis of MEG, EEG, and Invasive Electrophysiological Data. *Computational Intelligence and Neuroscience*, 2011.

[36] E. Pereda, R. Quian, and J. Bhattacharya. Nonlinear multivariate analysis of neurophysiological signals. *Prog. Neurobiol.*, 77:1–37, 2005.

[37] Jaap C Reijneveld, Sophie C Ponten, Henk W Berendse, and Cornelis J Stam. The application of graph theoretical analysis to complex networks in the brain. *Clin. Neurophysiol.*, 118(11):2317–31, November 2007.

[38] Mikail Rubinov, Stuart a. Knock, Cornelis J. Stam, Sifis Micheloyannis, Anthony W.F. Harris, Leanne M. Williams, and Michael Breakspear. Small-world properties of nonlinear brain activity in schizophrenia. *Hum. Brain Mapp.*, 30(2):403–416, February 2009.

[39] Mikail Rubinov and Olaf Sporns. Complex network measures of brain connectivity: uses and interpretations. *Neuroimage*, 52(3):1059–69, September 2010.

[40] V Sakkalis. Review of advanced techniques for the estimation of brain connectivity measured with EEG/MEG. *Comput. Biol. Med.*, 41(12):1110–7, December 2011.

[41] J.M. Schoffelen and J. Gross. Source connectivity analysis with MEG and EEG. *Human Brain Mapping*, 30(6):1857–1865, 2009.

[42] Siddharth S. Sivakumar, Amalia G. Namath, and Roberto F. Galn. Spherical harmonics reveal standing eeg waves and long-range neural synchronization during non-rem sleep. *Frontiers in Computational Neuroscience*, 10:59, 2016.

[43] Dirk J a Smit, Cornelis J Stam, Danielle Posthuma, Dorret I Boomsma, and Eco J C de Geus. Heritability of "small-world" networks in the brain: a graph theoretical analysis of resting-state EEG functional connectivity. *Hum. Brain Mapp.*, 29(12):1368–78, December 2008.

[44] C J Stam. Nonlinear dynamical analysis of EEG and MEG: review of an emerging field. *Clin. Neurophysiol.*, 116(10):2266–301, October 2005.

[45] C J Stam, W de Haan, a Daffertshofer, B F Jones, I Manshanden, a M van Cappellen van Walsum, T Montez, J P a Verbunt, J C de Munck, B W van Dijk, H W Berendse, and P Scheltens. Graph theoretical analysis of magnetoencephalographic functional connectivity in Alzheimer's disease. *Brain*, 132(Pt 1):213–24, January 2009.

[46] C.J. Stam. Functional connectivity patterns of human magnetoencephalographic recordings: a small-world network? *Neurosci. Lett.*, 355(1-2):25–28, January 2004.

[47] Cornelis J Stam, Guido Nolte, and Andreas Daffertshofer. Phase lag index: assessment of functional connectivity from multi channel EEG and MEG with diminished bias from common sources. *Hum. Brain Mapp.*, 28(11):1178–93, November 2007.

[48] C. E. Tenke and J. Kayser. Surface Laplacians (SL) and phase properties of EEG rhythms: Simulated generators in a volume-conduction model. *International journal of psychophysiology : official journal of the International Organization of Psychophysiology*, 97(3):285–298, September 2015.

[49] Frederik Van de Steen, Luca Faes, Esin Karahan, Jitkomut Songsiri, Pedro A. Valdes-Sosa, and Daniele Marinazzo. Critical comments on EEG sensor space dynamical connectivity analysis. *Brain Topography*, pages 1–12, 2016.

[50] Bernadette C M van Wijk, Cornelis J Stam, and Andreas Daffertshofer. Comparing brain networks of different size and connectivity density using graph theory. *PLoS One*, 5(10):e13701, January 2010.

[51] D. J. Watts and S. H. Strogatz. Collective dynamics of "small-world" networks. *Nature*, 393(6684):409–10, 1998.

[52] Van J. Wedeen, Patric Hagmann, Wen-Yih Isaac Tseng, Timothy G. Reese, and Robert M. Weisskoff. Mapping complex tissue architecture with diffusion spectrum magnetic resonance imaging. *Magnetic Resonance in Medicine*, 54:1377–1386, 2005.

List of Figures
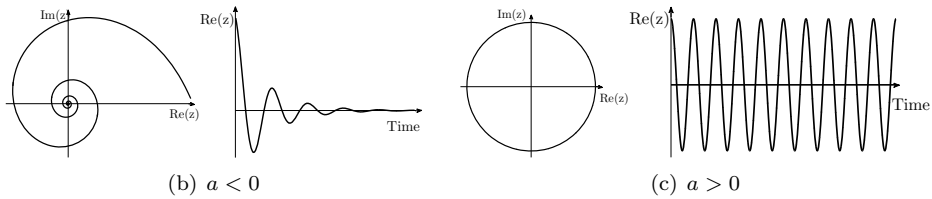
19

(a) Bifurcation parameter

(b) $a < 0$

(c) $a > 0$

Figure 1: (a) Impact of the bifurcation parameter a on the Hopf normal equation in (1). (b) For $a < 0$, the signal traces a spiral converging to zero in the complex plane, and a damped oscillation in the real domain. (c) For $a > 0$, the signal traces a circle in the complex plane and a self-sustained oscillation in the real domain.
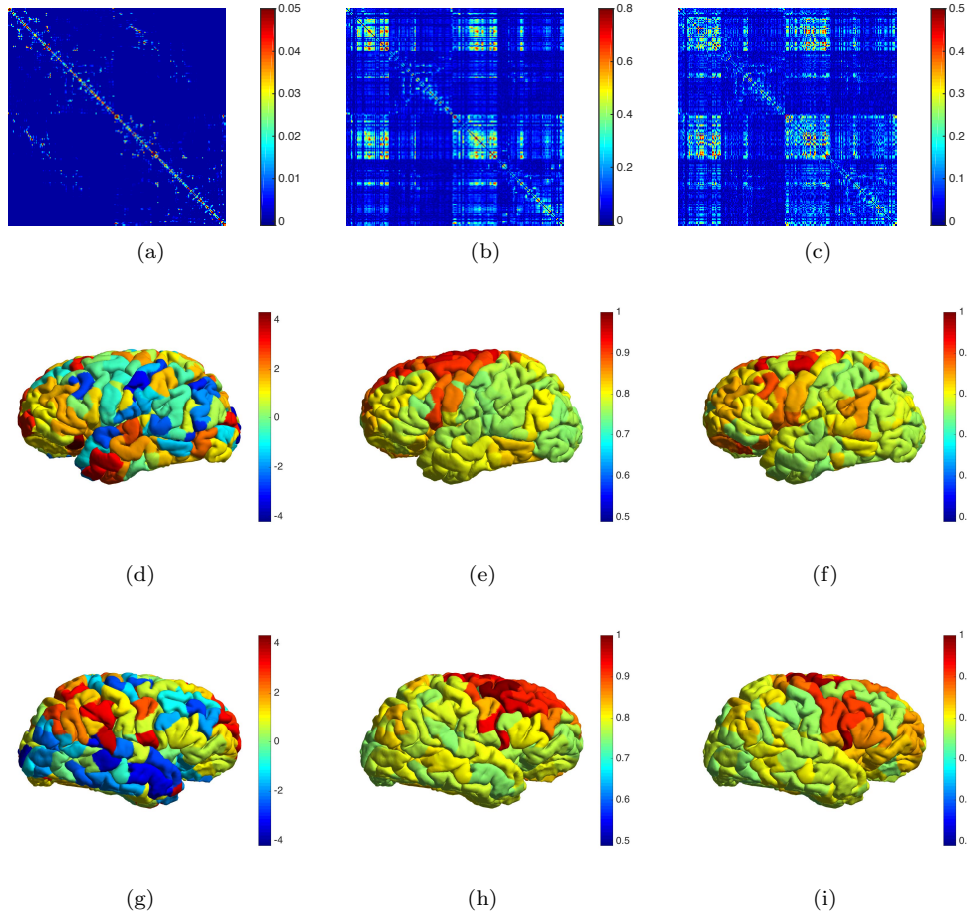
Figure 2: (a) Group-averaged (10 subjects) areal structural connectivity (S) matrix obtained using diffusion MRI fiber-tracking. (b) Instantaneous FC matrix RC_{cortex}. (c) Lagged FC matrix IC_{cortex}. (d), (g) A snapshot of simulated activity for the different areas in the cortical parcellation. (e), (h) Seed-based RC_{cortex} matrix (based on the right Caudal Middle Frontal). (f), (i) Seed-based IC_{cortex} matrix.
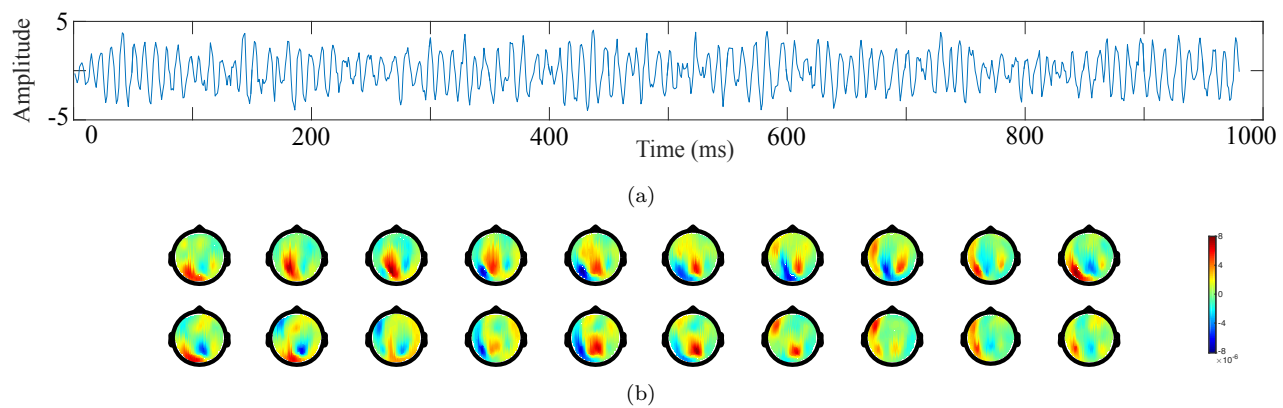
Figure 3: (a) Ten seconds of simulated cortical activity from a single area. (b) MEG axial signal image at sensor level for 20 samples, reported in intervals of 10 ms.
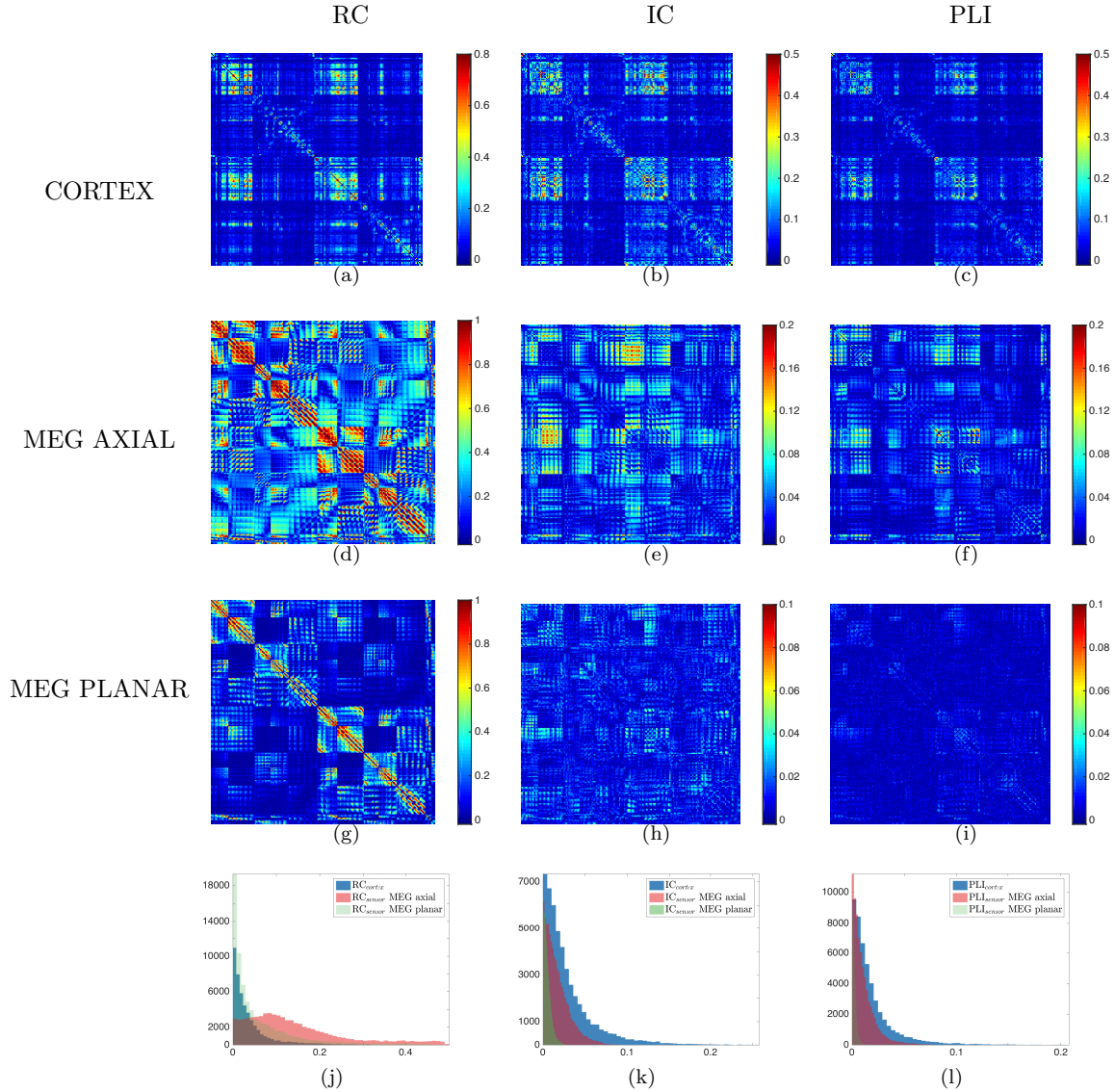
Figure 4: FC matrices at cortical-level: (a) Real correlation (RC_{cortex}), (b) Imaginary correlation (IC_{cortex}) and (c) Phase lag index (PLI_{cortex}). FC matrices at sensor level: (d) RC_{sensor} MEG axial, (e) IC_{sensor} MEG axial, (f) PLI_{sensor} MEG axial, (g) RC_{sensor} MEG planar, (h) IC_{sensor} MEG planar and (i) PLI_{sensor} MEG planar. Distribution of correlation values for (j) RC, (k) IC and (l) PLI at source and sensor level.
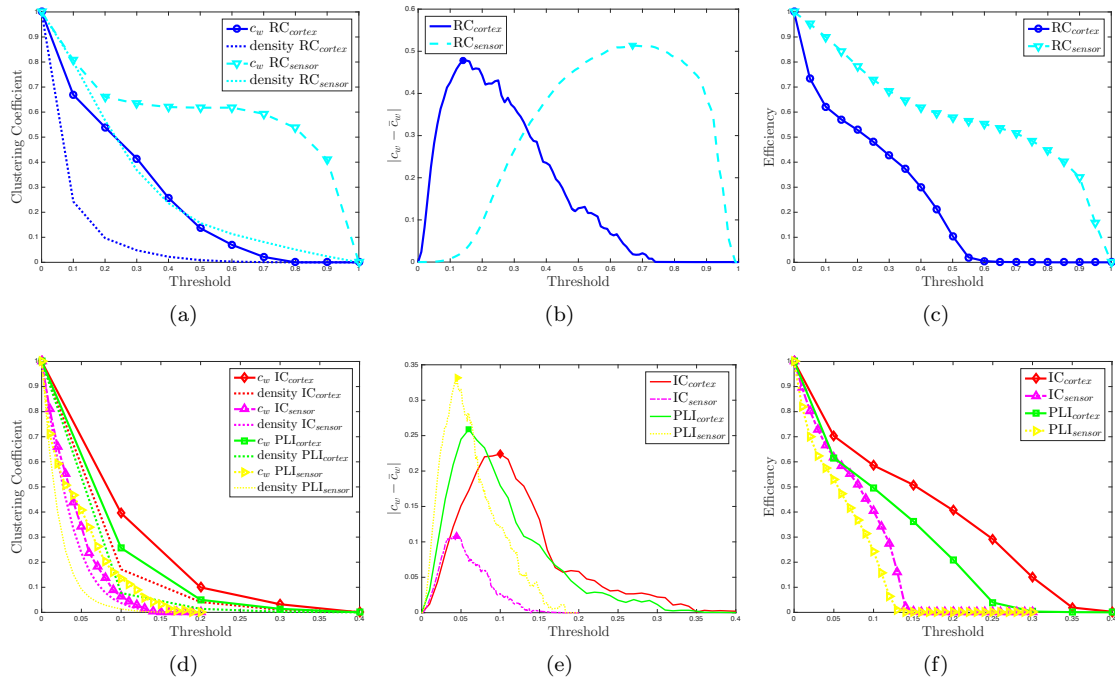
Figure 5: Network topologies for cortical and axial gradiometer resting-state networks. (a) Clustering coefficient as a function of the threshold for RC, (b) absolute difference with respect to a random network and (c) global efficiency vs. threshold. (d) Clustering coefficient as a function of the threshold for IC and (PLI), (e) absolute difference with respect to a random network, and (f) global efficiency vs. threshold for IC and PLI.
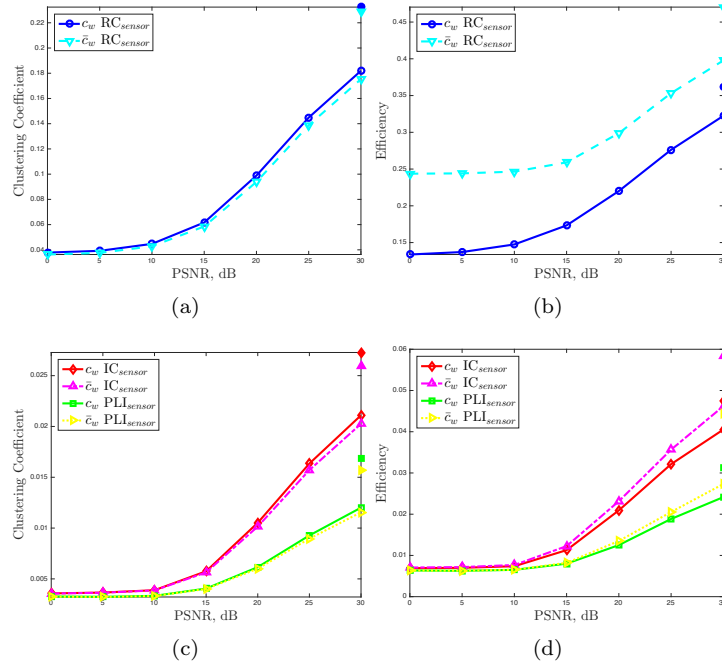
Figure 6: Effect of measurement noise-level for axial gradiometers. (a) Clustering coefficient vs. PSNR and (b) global efficiency for the RC matrices. (c) Clustering coefficient vs. PSNR and (d) global efficiency vs. PSNR for IC and PLI matrices. The results for the noise-free MEG data are marked with filled patterns.
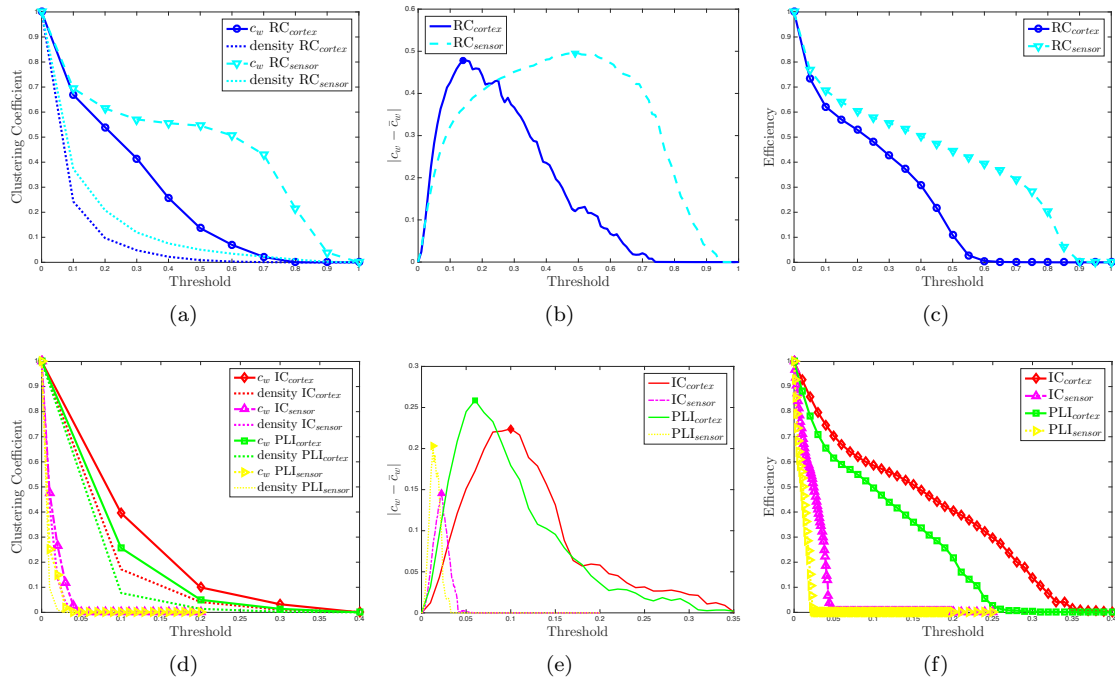
Figure 7: Network topologies for cortical and planar gradiometer resting-state networks.(a) Clustering coefficient as a function of the threshold for RC, (b) absolute difference with respect to a random network and (c) global efficiency vs. threshold. (d) Clustering coefficient as a function of the threshold for IC and (PLI), (e) absolute difference with respect to a random network, and (f) global efficiency vs. threshold for IC and PLI.
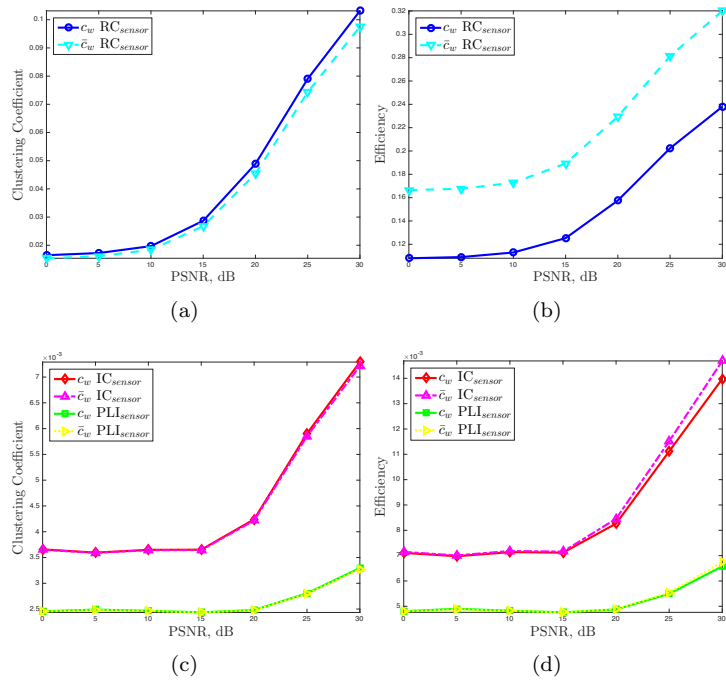
Figure 8: Effect of measurement noise-level for planar gradiometers. (a) Clustering coefficient vs. PSNR and (b) global efficiency for the RC matrices. (c) Clustering coefficient vs. PSNR and (d) global efficiency vs. PSNR for IC and PLI matrices.
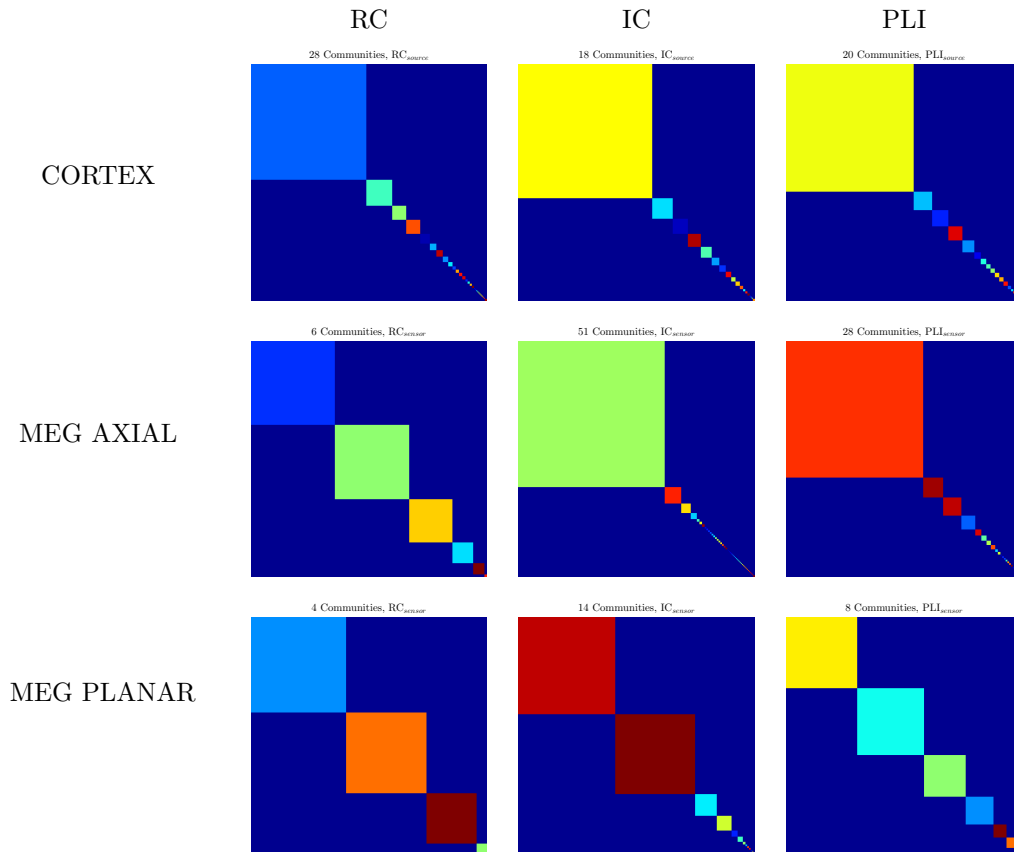
Figure 9: Louvain communities detected for every FC matrix and parameter resolution equal to 1 at source level (CORTEX), at sensor level with axial gradiometers (MEG AXIAL) and at sensor level with planar gradiometers (MEG PLANAR).
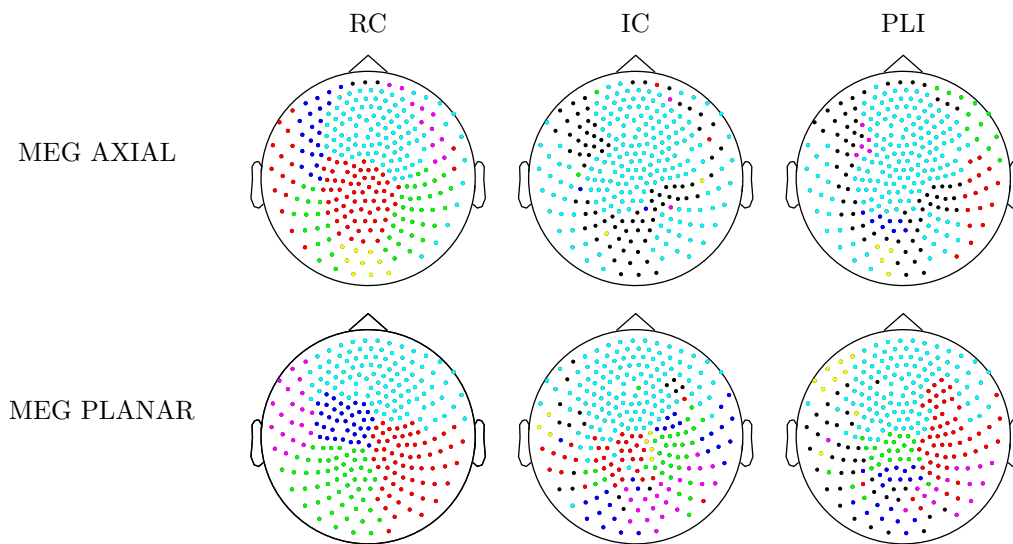
Figure 10: Map of detected communities onto the MEG helmet for RC_{sensor} axial, IC_{sensor} axial, PLI_{sensor} axial, RC_{sensor} planar, IC_{sensor} planar, and PLI_{sensor} planar.
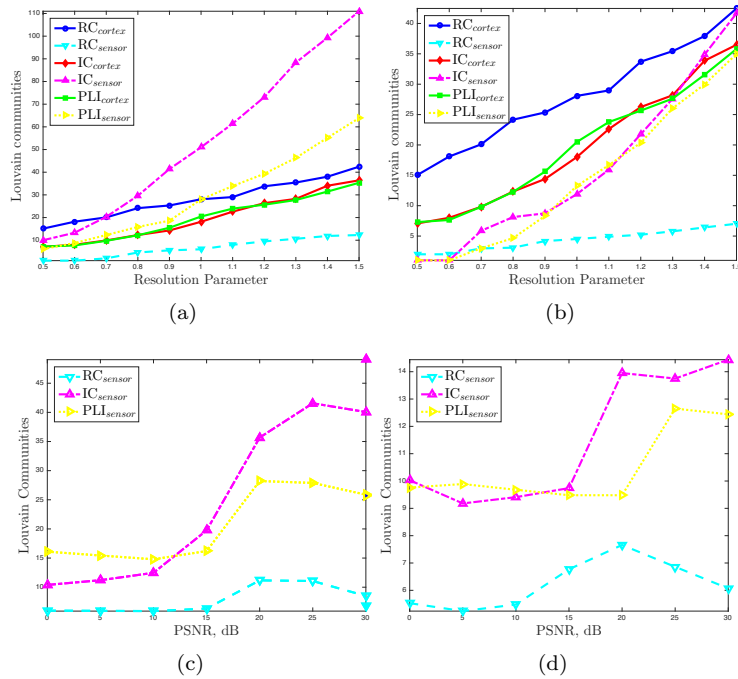
Figure 11: Number of communities detected for all FC matrices as a function of the resolution parameter for (a) the axial gradiometer MEG system and for (b) the planar gradiometer MEG system. Number of communities detected vs. PSNR obtained with the Louvain modularity algorithm with resolution parameter equal to one at sensor level for (c) the axial gradiometer MEG system and for (d) the planar gradiometer MEG system.